Solid Freeform Fabrication 2022: Proceedings of the 33rd Annual International
Solid Freeform Fabrication Symposium – An Additive Manufacturing Conference
Reviewed Paper

Thin-Walled Part Properties in PBF-LB/P — Experimental Understanding and Nonlocal Material Model

A. Jaksch[1,2], M. Spinola[1,3], C. Cholewa[1,2], L. Pflug[3,4], M. Stingl[1,3,4], D. Drummer[1,2]

[1]Collaborative Research Center - Additive Manufacturing (CRC 814), Friedrich-Alexander-Universität Erlangen-Nürnberg, Am Weichselgarten 10, 91058 Erlangen, Germany
[2]Friedrich-Alexander-Universität Erlangen-Nürnberg, Institute of Polymer Technology, Am Weichselgarten 10, 91058 Erlangen, Germany
[3]Friedrich-Alexander-Universität Erlangen-Nürnberg, Department of Mathematics, Chair of Applied Mathematics (Continuous Optimization), Cauerstr. 11, 91058 Erlangen, Germany
[4]Friedrich-Alexander-Universität Erlangen-Nürnberg, Competence Unit for Scientific Computing, Martensstr. 5a, 91058 Erlangen, Germany

Abstract

Understanding the mechanics, geometry effects, and process behavior of thin-walled components is critical to fully realizing the potential of lightweight design in powder bed fusion of polymers (PBF-LB/P). In this work, parts built with rectangular cross sections of different sizes and orientations are described by their geometry, surface roughness, mechanical characteristics, and specific component geometry dependent on energy input. Experimental findings are supported by a nonlocal material model developed to adequately describe weakened material behavior at the surface of PBF-LB/P parts. This approach allows the simulation of the elastic modulus and density for complex part geometries while simultaneously considering boundary effects. Furthermore, the volume-surface ratio for thin-walled components were linearly correlated to the rectangular cross sections in different building orientations. This uniformity indicates that this ratio is a suitable quantity to consider. Therefore, the process knowledge is improved, especially in new design standards for thin-walled structures in PBF-LB/P.

Introduction

Powder bed fusion of polymers is one of the most important processes in manufacturing lightweight designs and multifunctional parts. Due to the absence of support structures, nearly every design can be manufactured. In a lightweight design, small structures and features are used to transfer the resulting load to a bigger area. To realize the full potential of this kind of part, the mechanical performance of thin-walled features must be understood. Furthermore, this knowledge leads to the development of adapted material models to predict and optimize part properties in the designing process.

Because of the layerwise creation of the part geometry and the polymer powder's local melting, different boundary conditions affect the part creation process in the XY-plane and Z-direction [1]. In the XY plane, the smallest geometry possible is given by the laser spot diameter, for a CO_2-Laser this is 0.4-0.6 mm [2]. Recent machine developments are trying to reduce this spot diameter to manufacture even smaller structures in the future. The exposure strategy for the part geometry is split up in a contour scan, following the outer part geometry and a hatching scan melting the inner part of the geometry [3]. The hatching scan typically follows a meander scanning strategy, moving the scan lines parallel to each other with a given hatch distance [4]. Due to the Gaussian energy distribution in the laser focus, the hatch distance is chosen to be smaller than the halved laser spot diameter to achieve overlapping scan lines and a homogenous melt pool [5]. Additional exposure strategies (EOS Parameters: edge scan) with adapted laser power and scan speed are used for features smaller than the laser spot diameter [3]. Therefore, smaller features can be manufactured at the expense of geometry accuracy [6]. The energy is defined by the energy density, calculated from laser power, scan speed, and hatch distance. Due to the overlapping hatch lines, [7] determined that up to ten hatch lines are needed to achieve the calculated energy density in the process. Especially in small parts, this hatch number is not reached and therefore influences the energy input. Reference [8] proposed using a normalized energy density, calculated by the exposure area and total energy input for one layer. Further, normalized energy density was determined to be affected by the part orientation due to the change in the melt pool. Reference [9] showed that in the first layer, a melt pool is created deeper than the layer thickness, leading to an increased gap from the powder surface to the molten layer. This gap increased the theoretical layer thickness and melting volume in the next powder deposition. Up to twenty layers are needed to achieve a constant layer thickness. Furthermore, reference [10] demonstrated that the melt pool temperature rises over these first layers until it reaches a constant temperature. These effects influence part properties. Reference [8,11] showed that the mechanical properties are dependent on the part thickness; with reduced wall thickness, the mechanical properties, and density decrease nonlinearly. Aside from the explained effects, reference [8] proved with the help of CT-Measurements, that the surface roughness is independent of the part size. [12] observed the same behavior with roughness measurements. Due to the constant roughness, the impact of the surface increases with decreasing wall thickness.

The relevant material property is the elastic modulus. From a mathematical point of view, it is commonly modeled via the linear elasticity partial differential equation for small deformations (cf. [13]). From the resulting Hooke's Law, the corresponding set of equations yields a connection between elastic modulus, strains, and stresses acting on an arbitrary body. The wide usage of the model is explained by the possibility of supplementing it with a wide variety of boundary conditions and different levels of anisotropy for materials. Linear elasticity equations are also applied in the mathematical description of the material behavior of thin-walled parts (cf. [14, 15]). The elastic moduli resulting from the model are assumed to be constant, independent of the sizes of the body. However, as stated before, experiments have shown that a significant change in the mechanical behavior occurs, especially when decreasing the thickness of the part, which is not captured by the existing descriptions. A remedy for this modeling gap consists in using so-called convolutional integrals (cf. [16]) with appropriate integration kernels since these allow to obtain different material properties depending on the shape of a part.

This study aims to obtain a deeper understanding of these geometry effects. Therefore, parts with rectangular cross sections in different sizes and orientations are built and described by their geometry, surface roughness, mechanical characteristics, and the energy input as a function of the specific component geometry. Based on the experimental findings, a nonlocal material model is developed and calibrated, which adequately describes the observed weakened material behavior of thin-walled PBF-LB/P parts. Measurement data is used to fit the convolutional kernel in this nonlocal model. For the first time, this approach makes it possible to simulate the elastic modulus and density for complex part geometries under consideration of boundary effects.
This work further illustrates that the volume-surface ratio for thin wall constructions behave linearly in the case of rectangular cross sections in different building orientations, respectively. This uniformity indicates that the volume-surface ratio is a suitable quantity to consider. These findings increase the process knowledge, especially towards new design standards for thin-walled structures in PBF-LB/P.

Materials and Methodology

Material and machine

Polyamide 12 (PA12) powder (PA 2200, EOS GmbH, Krailling, Germany) is used for the experiments. The powder is mixed according to the manufacturer's recommendation, 50 wt.-% used powder and 50 wt.-% virgin powder. Prior to experiments, the powder was characterized. The powder system's bulk density (0.44 ± 0.01 g/cm³) and the viscosity number (79 ± 1.0 ml/g) and particle size distribution (d10,3 = 45,7 µm, d50,3 = 62,7 µm, d90,3 = 83,7 µm) were measured. The experiments are carried out with an EOS P396 from EOS GmbH. The machine uses a 70 W CO2-Laser with a 0.6 mm laser focus diameter.

Test specimen and processing parameters

Adapted tensile test samples based on DIN EN ISO 527 are built with six different wall thicknesses (0.5, 1.0, 1.5, 2.0, 3.0, and 4.0) in the three main orientations, xy, xz, and z-direction (Fig. 1). The build job layout is shown in Fig. 2 (left). Over the z-direction, the layout is sorted by the part orientation leading in total to 336 parts (144 xy, 96 xz, and 96 z-direction), and a filling degree of 4 vol.-%. The parts are scaled in the pre-processing according to the values shown in Fig. 2 (right). A quality build job layout determines the scaling parameters by EOS GmbH for the used powder mixture and building temperatures.

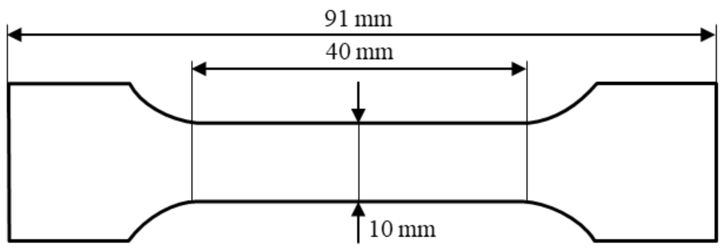

Fig. 1: Tensile test sample based on DIN EN ISO 527

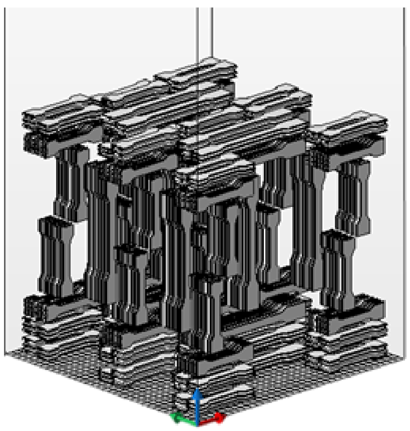

Direction	**Scaling value**
x-Scaling	3.02 %
y-Scaling	2.97 %
z(0mm)-Scaling	2.6 %
z(300mm)-Scaling	2.0 %
z-Compensation	0.12 mm
Parameter	**Setting**
Build chamber temperature	174 °C
Removal chamber temperature	130 °C
Layer thickness	0.12 mm
Building height	310 mm
Beam offset	0.3 mm

Fig. 2: Build job layout (left), scaling, and process parameters (right)

Processing parameters used are shown in Fig. 2 (right). For exposure, the EOS Parameters for PA 2200 and 0.12 mm layer thickness are used (PA2200_120_111). The parameters use a contour scan, a layerwise alternating hatch in x and y-direction, and an edge setting for exposure areas smaller than the laser focus diameter in the experiments for the 0.5 mm parts.

After printing, the parts are carefully cleaned with a brush, and post-processed via glass bead blasting. For the blast process, a Wiwox DI 12 machine is used for 3 minutes with a blasting pressure of 3 bar and glass beads between 100 – 200 µm. After cleaning, the parts are immediately stored in a vacuum to maintain the dry conditioning for mechanical testing.

Analysis methods

To better understand the wall-thickness effects, the normalized energy input is calculated according to [8] by the total energy input and the cross section shown in the pre-processing software PSW 3.8 EOS P396. For each layer and part, the energy input in the middle area of the tensile bar is evaluated by the planned scan path (Fig. 3, right). Therefore, the total contour, hatch, and edge exposure lengths are measured, and the total energy input for each layer is calculated. This total energy input is then normalized by the exposure area. The result is further normalized with respect to the xy-orientation.

Fig. 3: Measuring position for the part geometry (left) and evaluation area for the surface roughness and energy input (right)

The part thickness and width are measured with a micrometer at three sample positions for the geometry. Additionally, the part is digitalized by a scanner (Canon 9000F) with a resolution of 1200 DPI (Pixelsize 21.17

µm), and the part area is calculated with the python library OpenCV. The part weight is measured (Mettler Toledo, AX105DR), and the density is calculated by the part area, thickness, and weight.
A 3D-Scanner Comet L3D 2 with a C45 objective lens (Carl Zeiss AG, Oberkochen, Germany) is used to evaluate the surface roughness. Based on the 3D-Scans, the average surface roughness (Sa) of the primary surface is calculated by MountainsLab 9.1 (Digital Surf, Besançon, France).
Mechanical testing is performed according to DIN EN ISO 527-1 [17] and -2 [18]. A tensile testing machine of Type 1484 (Zwick Roell, Ulm Germany), with an extensometer, is used. The Young's modulus is measured with a testing speed of 0.5 mm/min and 0.25 % deformation. The elongation at break is measured at 25 mm/min. The clamping length is set to 62 mm.

Results and Discussion

In relation to the orientation, the theoretical melt pool size differs strongly (Fig. 4, left). While the xy-orientation shows the biggest exposure area, it is independent of the part thickness and created by the layer number. For the xz-orientation, a long and small exposure area is created, with a direct correlation between the theoretic melt pool size and the thickness. While the contour scan length changes only a little, the number of hatch lines reduces with decreasing part thickness. This applies to the z-oriented parts as well. The hatch grid is essential, especially for the xz and the z-orientation; due to a fixed hatch distance, the hatch line number depends on the part position in the xy-plane. The exposure parameters use an alternating hatching strategy, changing the direction of the scan vector by 90° with every layer. This leads to a layer-depending effect. If the hatch line is vertically oriented to the part thickness, the vector length only slightly changes; however, if the hatch line is horizontal to the thickness, the number of hatch lines varies significantly.
Furthermore, the part position affects the scan pattern due to the hatch grid. Fig. 4 middle illustrates a 3 mm z-oriented part with the green lines representing the hatch lines. The same part size can have seven or eight hatch scans, influencing the energy input of each layer. These effects are observed for each thickness and increase with decreasing part thickness
Based on this data, (Fig. 4, left) shows the calculated normalized energy density (NED). Because of the constant exposure area of the xy-part, the NED is constant for all parts thicknesses, and therefore used as a reference. For the xz and z-oriented parts, a decrease of the NED is observed for parts thinner than 2 mm.
Furthermore, a decrease of the NED in the 3 mm part is observed. This is explained due to an error in the part placement, resulting in 7 hatch lines instead of 8 hatch lines. A low energy density can lead to a not fully molten powder [5]. But further work suggests that the resulting melt pool temperature depends not only on the energy density but on additional parameters e.g., the decay time [19].

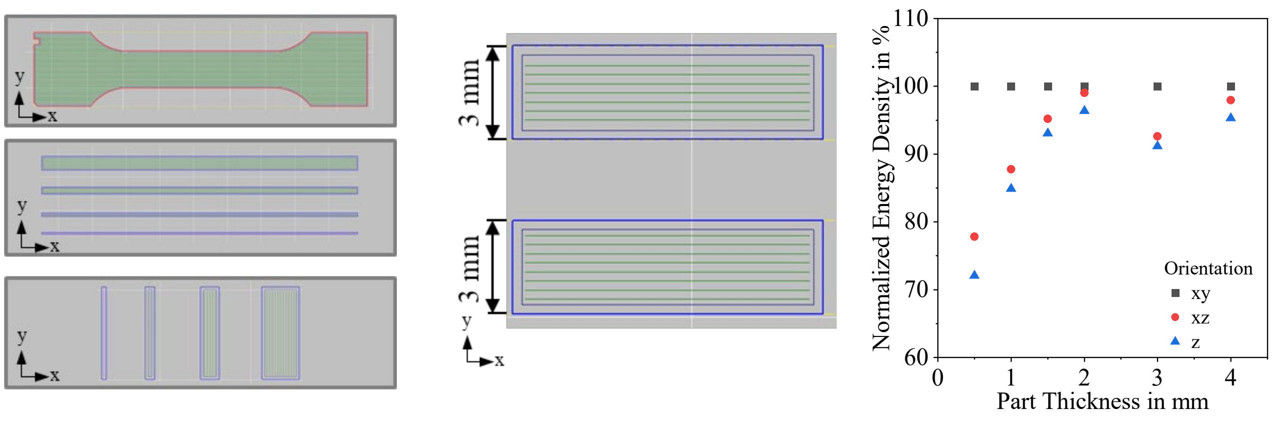

Fig. 4: Scan strategy depending on the orientation and wall thickness (left), hatch grid and position (middle), normalized energy density (left)

The dimensional accuracy is of high importance for thin-walled parts. Fig. 5 left shows the dimensional deviation of the part thickness. Parts in xy-orientation exhibit a constant offset of 0 – 5 % independent of the set part thickness. The layer number that generates the thickness is not freely scalable. For xz and z-oriented parts, an increase in the dimensional deviation is observed for parts smaller than 2 mm. The 0.5 mm parts show a sharp increase in the deviation, up to 25 %, so the machine cannot produce accurate parts in this thickness due to the laser spot diameter of 0.6 mm. Compared to the thickness, the width of the parts (Fig. 5 middle), which is set to 10 mm for all parts, shows a higher accuracy. This results in a cross section deviation, which mainly depends on the dimensional deviation of the part thickness. Overall, all parts have a larger cross-section than the defined dimension.

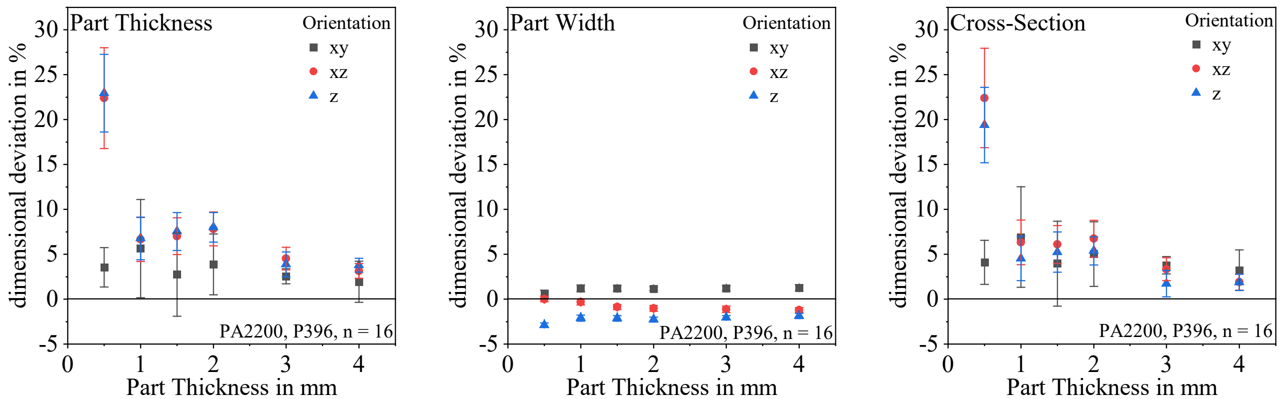

Fig. 5: Dimensional accuracy of the thickness, width, and cross section depending on the part thickness

Due to the tactile measurement of the dimension, the surface roughness leads to a systematic measuring error [8]. Fig. 6 left shows the parts' average surface roughness (Sa). For xz and z-orientation, no significant difference of the orientation nor the part thickness is observed. Overall, the xy-oriented parts display a lower average roughness. For the 0.5 mm xy-oriented parts, a slight increase in the roughness can be detected. This part consists of only three layers. [10] showed that up to 20 layers are necessary to build up a homogenous temperature field. Due to lower temperatures, the particles may not melt up ideally, leading to increased roughness.
The part density (Fig. 6, right) correlates with the part thickness. With lower thickness, the density decreases as the constant surface roughness leads to a significant increase in the surface area with decreasing wall thickness. This volume does not contribute to the density or the mechanical properties. [8] showed with CT measurements that the porosity volume is decreasing with the part thickness; therefore, the main effect of this nonlinear behavior is the surface which must be included in the design process.

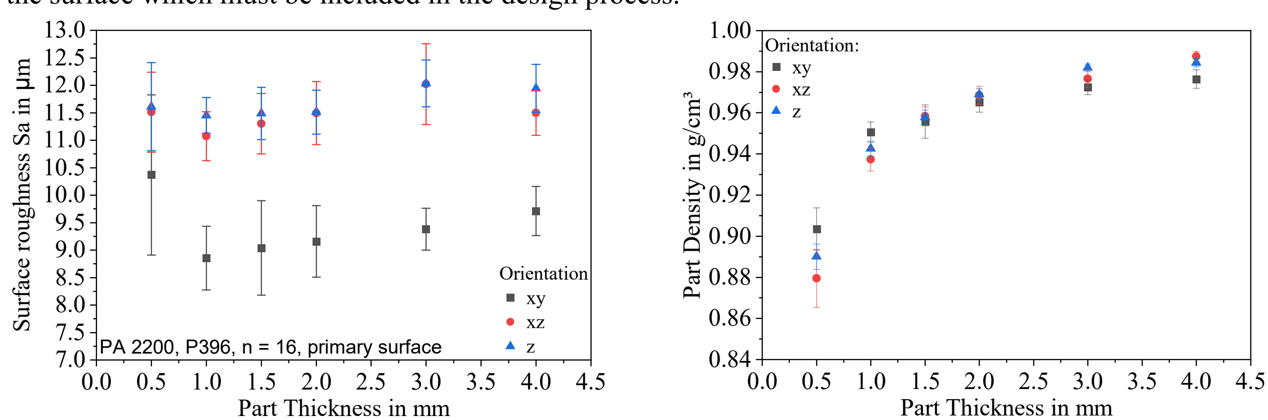

Fig. 6: Surface Roughness (left) and Part Thickness (right)

The dimensional accuracy, surface roughness, and part density influence the mechanical properties depict in Fig. 7. The apparent Young's modulus (Fig. 7, left) and the tensile strength (Fig. 7, middle) show a similar trend. With decreasing part thickness, mechanical properties decrease nonlinearly. The z-oriented parts show the highest E-Modules, while the xy and xz-oriented parts are the same values. A higher decrease of the modulus for the z-parts is detected for only the 0.5 mm parts. This part thickness is too small for the laser focus diameter and is therefore molten with an edge scan. This scanning parameter uses, in theory, lower energy parameters. Overall, the tensile strength shows the same part behavior. More parameters, e.g., surface defects or pores, must be considered for the breaking behavior. The elongation at break is therefore highly sensitive to the processing parameters, material, and part properties. While the xy and xz-oriented parts show close to the same elongation at break (Fig. 7, right), the z-orientation is significantly lower. Furthermore, xz and z-oriented parts demonstrate a slight drop for the 3 mm parts. Due to the hatch grid, these parts do not contain the maximum number of hatch lines, leading to lower temperatures and influencing the polymer powder's melting. Furthermore, for the xz and xy-oriented parts, a decrease of the elongation at break for parts smaller than 2 mm is observed.

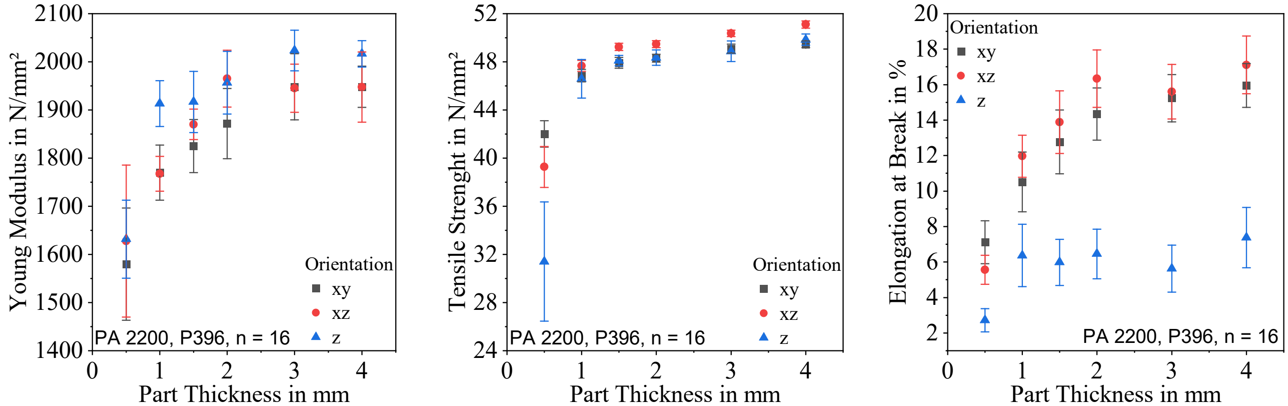

Fig. 7: Mechanical Properties dependent on the part thickness, apparent Young's modulus (left), tensile strength (middle) and elongation at break (right)

While the density and the mechanical properties show a nonlinear behavior to the part thickness, the surface roughness exhibits no such effect. The surface-to-volume area is a possible parameter to describe the relationship between the surface and the volume. Therefore, this parameter is used for a better understanding of the behavior of thin-walled parts. Fig. 8 left shows the part density, where a linear dependency of the density, and the surface-to-volume area is detected. The same applies to the Young's modulus (Fig. 8, right). Furthermore, the results show a difference between the xy and the xz and z parts. Generally, the surface-to-volume area is a suitable parameter to describe the part behavior of thin-walled PBF-LB/P parts. The necessary number of experiments is reduced with the linear behavior to evaluate the material properties of new materials. However, for more complex part geometries and part optimization, adapted material models are needed to describe the boundary effects of PBF-LB/P parts.

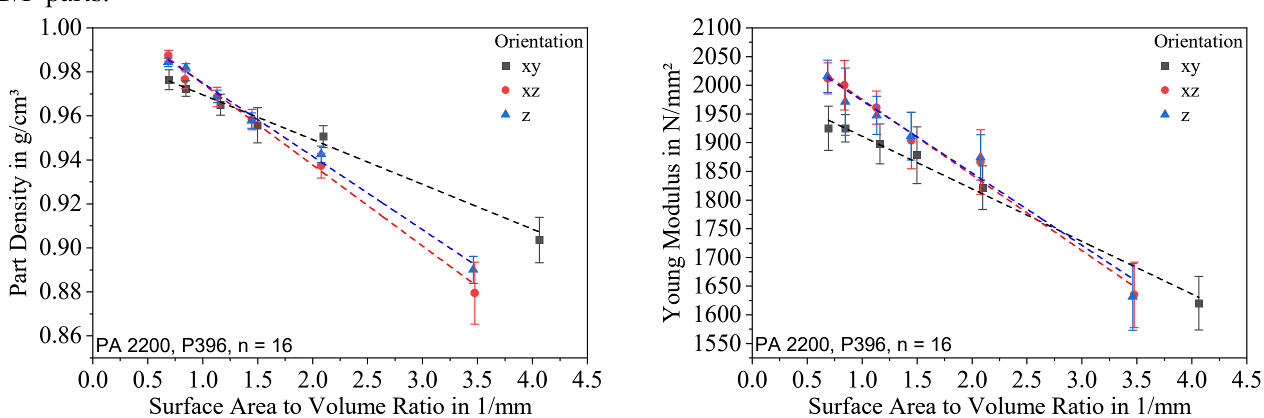

Fig. 8: Part density (left) and apparent Young's modulus (right) dependent on the surface area to volume ratio

<u>Nonlocal Material Model and Validation with Measured Data</u>

Mathematical model

This section focuses on the derivation of a suitable mathematical formulation of the observed behavior of thin-walled parts. As mentioned in the introduction, the part thickness dependent change in the elastic modulus is explained by the extent of boundary effects that occur at the surface of the body, which is depicted in the subsequent Fig. 9.

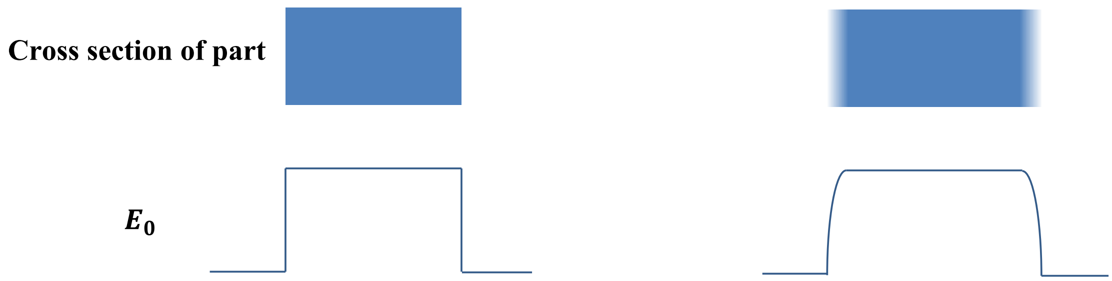

Fig. 9: Constant material behavior, i.e., bulk (left). Bulk material in the inner region of the part and weakened material behavior at the surface (right)

The illustrated material behavior of the elastic modulus at a location $\boldsymbol{x} \in \mathbb{R}^3$ in space, especially near its boundary, is mathematically represented by the following so-called convolution term (cf. [16])

$$E_\rho(\boldsymbol{x}) := \frac{E_0}{C_{\text{specimen}}} \rho(\boldsymbol{x}) \int_{\mathbb{R}^3} \psi_r(\boldsymbol{y} - \boldsymbol{x}) \rho(\boldsymbol{y}) \mathrm{d}\boldsymbol{y}.$$

Here, $E_\rho(\boldsymbol{x})$ denotes the elastic modulus of the part with bulk density ρ in $\boldsymbol{x}$, E_0 the elastic modulus of the bulk density, C_{specimen} the upper convolutional integral at the standard specimen with a 10 mm $\times$ 4 mm rectangular cross section. The term ψ_r describes a convolution kernel with spherical support of radius $r > 0$. The modeling via the introduced convolution is motivated by the non-uniform heat distribution in a part during the laser sintering process. The integration kernel yields the desired effect: When computing the elastic modulus at a point in space outside the part, then the considered part density is 0, and thus the elastic modulus vanishes there. For points that are inside the part and sufficiently distant from the boundary, then the full density contributes to the integral, leading to the bulk density there. For points near the boundary, the integration kernel considers both points within and outside of the part leading to an intermediate value for the elastic modulus.
In this publication, the following, normalized with respect to integration, radially symmetric integration kernel ψ_r (cf. [20, p. 14]) is used, which decreases linearly when approaching the boundary of the observation sphere

$$\psi_r(\boldsymbol{x}) := \frac{3}{\pi r^3} \max\left\{1 - \frac{||\boldsymbol{x}||_2}{r}, 0\right\}.$$

Further, especially in view of a suitable comparison with the measurements illustrated in the previous sections, the average elastic modulus $E_{\rho,\text{mean}}$ over the whole part Ω will be considered (cf. [21, p. 361]), i.e.,

$$E_{\rho,\text{mean}} := \frac{1}{\text{vol}(\Omega)} \int_\Omega E_\rho(\boldsymbol{x}) \mathrm{d}\boldsymbol{x}$$

where $\text{vol}(\Omega)$ denotes the volume of the part. In general, the computation of $E_{\rho,\text{mean}}$ would require the calculation of integrals in a three-dimensional space. However, due to the here considered cuboid geometry of the part and the radially symmetric convolution kernel ψ_r, it is possible to reduce the computation to integrals in $\mathbb{R}^2$. This is an advantage when it comes to a numerical approximation of the integrals, as it will be done in this publication. A reduction of dimensions leads to a more accurate approximation with the same number of discretization points, and thus to a faster, more efficient numerical scheme (cf. [22]).
Here, due to the cuboid geometry of the part, the density ρ is constant along one direction, for simplicity the z-direction. Thus, the density $\hat{\rho}$ is considered in the following, which is defined as $\hat{\rho}(x, y) := \rho(x, y, z)$ for every $(x, y, z) \in \mathbb{R}^3$. Further, instead of ψ_r an equivalent integration kernel $\hat{\psi}_r$ defined on $\mathbb{R}^2$ is considered, namely by an appropriate change of variables with cylindrical coordinates (cf. [23, p. 252] and [24]). The surrogate term

$$\hat{\psi}_{r,\text{cylindrical}}(\tau,\varphi) := \int_{-\sqrt{r^2-\tau^2}}^{\sqrt{r^2-\tau^2}} \psi_r(\tau\cos\varphi, \tau\sin\varphi, z)\mathrm{d}z$$

yields the corresponding, equivalent kernel $\hat{\psi}_r$ in Cartesian coordinates

$$\hat{\psi}_r(x,y) := \frac{3}{\pi r^3}\max\left\{\sqrt{r^2-(x^2+y^2)} - \frac{(x^2+y^2)}{r}\sinh^{-1}\left(\frac{\sqrt{r^2-(x^2+y^2)}}{\sqrt{x^2+y^2}}\right), 0\right\}.$$

The previous computations lead to

$$E_\rho\big((\hat{\boldsymbol{x}},z)\big) = \hat{E}_\rho(\hat{\boldsymbol{x}}) := \frac{E_0}{C_{\text{specimen}}}\rho(\hat{\boldsymbol{x}})\int_{\mathbb{R}^2}\hat{\psi}_r(\hat{\boldsymbol{y}}-\hat{\boldsymbol{x}})\rho(\hat{\boldsymbol{y}})\mathrm{d}\hat{\boldsymbol{y}}$$

and thus

$$E_{\rho,\text{mean}} = \hat{E}_{\rho,\text{mean}} := \frac{1}{\text{area}(\Omega_{\text{cs}})}\int_{\Omega_{\text{cs}}}\hat{E}_\rho(\hat{\boldsymbol{x}})\mathrm{d}\hat{\boldsymbol{x}}$$

where Ω_{cs} is the rectangular cross section of Ω and $\text{area}(\Omega_{\text{cs}})$ its area.

Simulation and validation with measurements

After describing the nonlocal material model, the average elastic modulus for different parts is computed and compared with the experiments. Due to the considered radially symmetric integration kernel, differences in the building directions are not regarded in this case. Thus, measurements for every considered width of the rectangular cross section are aggregated respectively. Further, the integrals are of a convolutional type such that it allows an efficient numerical approximation via a Fast Fourier Transform (cf. [25]). The result is illustrated in Fig. 10.

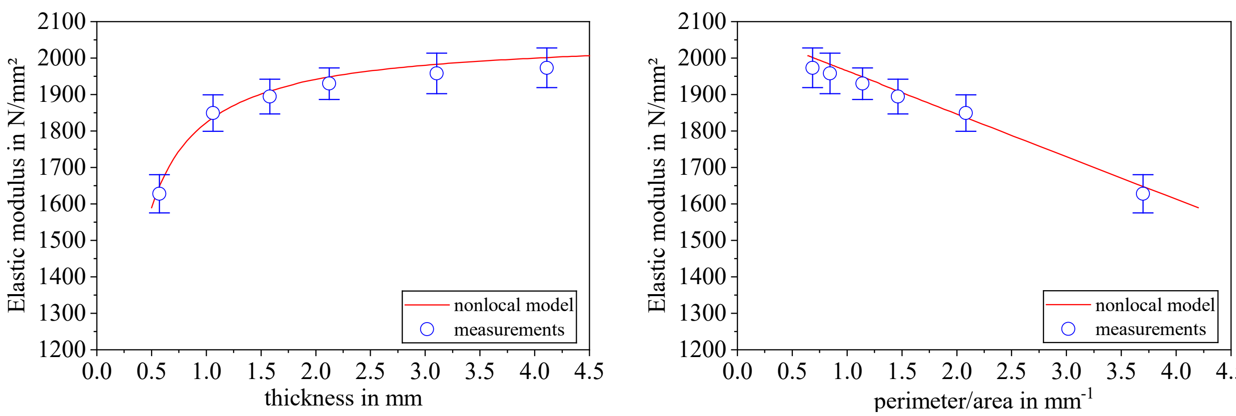

Fig. 10: Comparison of simulated elastic modulus (red) with the respectively averaged measurements (blue). Standard deviations are illustrated with error bars, respectively. Plot with respect to thickness (left) and with respect to the perimeter to area ratio (right)

As shown in Fig. 10, the simulated results are contained within every interval given by the mean value of the measurements and the standard deviation. Thus, an adequate description of the elastic modulus of thin-walled parts is given. Since the simulated mean elastic modulus depends on the radius r of the integration kernel, the following approach was used to obtain a suitable radius. For simplicity, radii within the interval $(0,1)$ were considered. Now, the radius was chosen such that the typically chosen least-squares minimization task was tackled. I.e., the distance of the vector containing n measured elastic moduli $(E_{k,\text{measurements}})_{k=1,\dots,n}$ to the radius depending on simulated ones $(E_{\rho_k,\text{mean}}(r))_{k=1,\dots,n}$ was minimized (cf. [26]). The difference is given by the subsequent term J as a function of the radius r

$$J(r) := \sqrt{\sum_{k=1}^{n} |E_{\rho_k,\mathrm{mean}}(r) - E_{k,\mathrm{measurements}}|^2}.$$

The J minimizing radius r, which fulfills $r \approx 0.4$, was approximated by a bisection scheme (cf. [25]). Motivated by Fig. 11, a binary search in the interval $(0,1)$ was performed, and for a sufficiently small given threshold $\varepsilon_1 > 0$ the finite differences $\frac{1}{-\varepsilon_1}(J(r-\varepsilon_1) - J(r))$ and $\frac{1}{\varepsilon_1}(J(r+\varepsilon_1) - J(r))$ were calculated. If in the considered iteration both are negative/positive, r is smaller/larger than the optimal one. If the terms possess a different sign or if the absolute value of the finite differences is smaller than a second given error tolerance ε_2, the algorithm terminates.

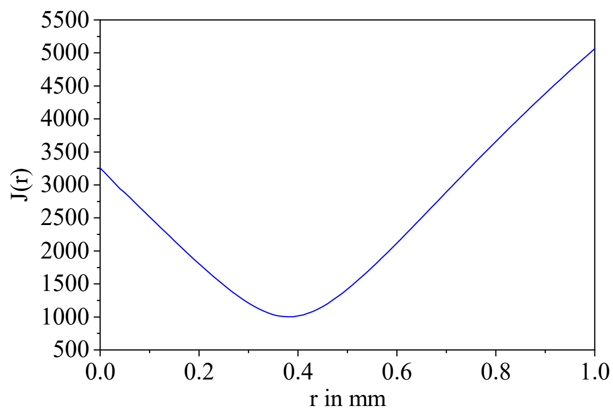

Fig. 11: Plot of J representing a least-squares task to obtain an adequate radius for the integration kernel

Linear behavior of elastic modulus with respect to the ratio of surface area and volume

As observed in Fig. 8, the measured elastic moduli follow a linear behavior regarding the part's surface area to volume ratio. According to the previous results, it is analogously related to the perimeter to surface area ratio δ of the cross section. The following discussion shows that this is explained by the here-stated nonlocal material model. In Fig. 12 a rectangular cross section with sides a and b with $a < b$ is considered. Here, the radius r of the integration kernel fulfills $2r \leq a$. The mentioned ratio δ corresponds to

$$\delta = \frac{2(a+b)}{ab} = 2\left(\frac{1}{a} + \frac{1}{b}\right).$$

The goal is to show that there exist constants $c_1 \geq 0$ and $c_2 \leq 0$ such that

$$E_{\rho,\mathrm{mean}} = c_1 + c_2\delta.$$

Due to the positive radius of the circular support of the integration kernel, the calculation of $\hat{E}_{\rho,\mathrm{mean}}$ is split into the several areas $A_1, \dots, A_4$. Together with the linearity of the integral, it holds that

$$\int_{\Omega_{\mathrm{cs}}} \hat{E}_\rho(\hat{\boldsymbol{x}})\mathrm{d}\hat{\boldsymbol{x}} = \int_{A_1} \hat{E}_\rho(\hat{\boldsymbol{x}})\mathrm{d}\hat{\boldsymbol{x}} + 2\int_{A_2} \hat{E}_\rho(\hat{\boldsymbol{x}})\mathrm{d}\hat{\boldsymbol{x}} + 2\int_{A_3} \hat{E}_\rho(\hat{\boldsymbol{x}})\mathrm{d}\hat{\boldsymbol{x}} + 4\int_{A_4} \hat{E}_\rho(\hat{\boldsymbol{x}})\mathrm{d}\hat{\boldsymbol{x}}.$$

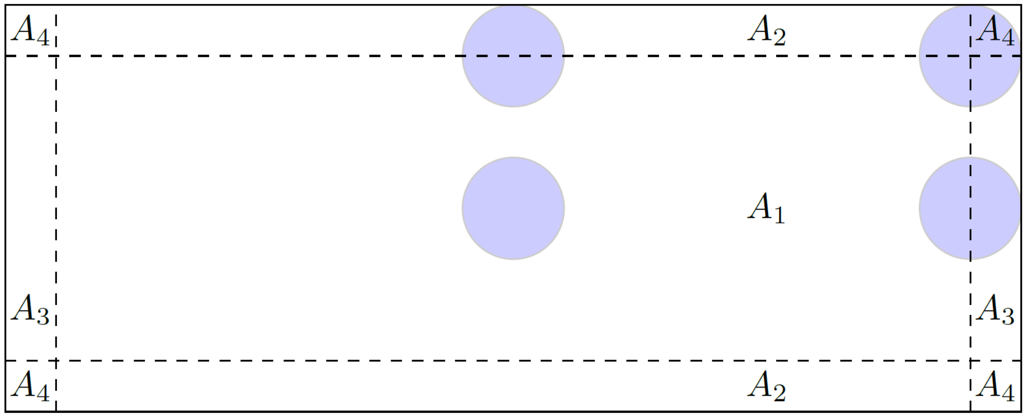

Fig. 12: Rectangular cross section of part together with different located integration kernels which are denoted by blue circles with radius r. Depending on the several areas $A_1, \ldots, A_4$, different behaviors of the elastic modulus occur

In the region A_1, the full density ρ will be considered such that the first integral is $(a-2r)(b-2r)$. For the second integral, the two-dimensional integral can be rewritten as two iterated, one-dimensional integrals (cf. [27, p. 247]). Since the elastic modulus does not change along the direction of the longer side, within the bosy it holds that

$$\frac{C_{\text{specimen}}}{E_0}\int_{A_2} \hat{E}_\rho(\hat{\boldsymbol{x}})\mathrm{d}\hat{\boldsymbol{x}} \;=\; \frac{C_{\text{specimen}}}{E_0}(b-2r)\int_0^r E_\rho\left(\frac{b}{2},\tau\right)\mathrm{d}\tau \;=:\; (b-2r)I_1.$$

Analogously, it is valid

$$\begin{aligned}\frac{C_{specimen}}{E_0}\int_{A_3} \hat{E}_\rho(\hat{\boldsymbol{x}})\mathrm{d}\hat{\boldsymbol{x}} \;&=\; \frac{C_{\text{specimen}}}{E_0}(a-2r)\int_0^r E_\rho\left(\tau,\frac{a}{2}\right)\mathrm{d}\tau\\ &=\; \frac{C_{\text{specimen}}}{E_0}(a-2r)\int_0^r E_\rho\left(\frac{b}{2},\tau\right)\mathrm{d}\tau \;=\; (a-2r)I_1.\end{aligned}$$

By denoting

$$I_2 := \frac{C_{\text{specimen}}}{E_0}\int_{A_4} \hat{E}_\rho(\hat{\boldsymbol{x}})\mathrm{d}\hat{\boldsymbol{x}},$$

it yields

$$\begin{aligned}E_{\rho,\text{mean}} &= \frac{E_0}{C_{\text{specimen}}}\frac{(a-2r)(b-2r)+2(b-2r)I_1+2(a-2r)I_1+4I_2}{ab}\\ &= \frac{E_0}{C_{\text{specimen}}}\left[1-\frac{f}{b^2}+\left(I_1-r+\frac{f}{2b}\right)\delta\right]\end{aligned}$$

with $f \;:=\; 4(r^2+I_2)-8rI_1$. Due to the normalization of the integration kernel, it holds that $I_2 \le rI_1$ and $I_1 \le r$ such that $1-\frac{f}{b^2} \ge 0$ and $I_1 - r + \frac{f}{2b} \le 0$. Thus, the observed linear behavior in experiments for the here considered geometry for $2r < a$ is mathematically proven.

Summary and Outlook

This work showed that the energy input for thin-walled parts significantly depends on the orientation, the wall thickness, and the hatch grid, in turn affecting the pre-processing of the build job. Although scaling parameters are used, which were evaluated for the used powder mixture and building temperature, all parts show a bigger cross-section than defined. This deviation resulted from a dimensional error of the set thickness. The surface roughness is mainly independent of the part thickness and leads to an increased error for smaller parts, which leads to a nonlinear decrease in the part density and the elastic modulus. The surface area to volume ratio is used to consider the surface roughness, leading to linear part behavior.

The core of the nonlocal material model presented in this publication consists of the integral kernel in a convolution term. By this, boundary effects, and thus the observed weakened material behavior at the surface of parts, are captured mathematically. In this work, a radially symmetric, linear integration kernel was used. The convolutional terms were computed numerically by a Fast Fourier Transform algorithm for an efficient approximation. The obtained simulations agreed with high accuracy to the measurements after having derived an optimal radius for the sphere of action of the integration kernel. Moreover, by splitting the considered rectangular cross-section geometry of the part into appropriate sectors, the observed linear behavior of the elastic modulus regarding the surface area to volume ratio was proven mathematically. This yields a more comprehensive understanding of thin-walled structures and their material design.

From a mathematical point of view, the nonlocal material model can be modified in different ways to obtain an even more accurate description and improved understanding of the behavior of thin-walled parts. In the following, three of the several aspects which are worth investigating in future research are described. First, even though only cuboid structures were analyzed in this publication, the mathematical description can also be applied to a vast range of other geometries, e.g., specimen with circular or elliptical cross sections. Measurements for these further geometries can be fed into the nonlocal material model to calibrate the radius of the integration kernel. Second, another extension of the derived results consists in substituting the linear integration kernel with a nonlinear one. By this, the extent of the simulated boundary effects can vary and adapt according to the experiments. Third and finally, while the mathematical model in this publication considered a radially symmetric and isotropic integration kernel, using an anisotropic kernel that weights boundary effects depending on the directions to a different extent is reasonable. This allows capturing the here illustrated, in experiments visible effect of the construction direction to the elastic modulus also in the mathematical description.

Acknowledgment

Funded by the Deutsche Forschungsgemeinschaft (DFG, German Research Foundation) – Project-ID 61375930 – SFB 814, sub-project T3, A3. In addition, the authors want to thank the companies EOS GmbH and 1zu1 Prototypen GmbH & Co KG for their cooperation and support.

References

[1] M. Schmid, Laser sintering with plastics: technology, processes, and materials, First edition, Hanser Publishers ; Hanser Publications, Cincinnati : Munich, 2018.

[2] D. Drummer, M. Drexler, K. Wudy, Derivation of Heating Rate Dependent Exposure Strategies for the Selective Laser Melting of Thermoplastic Polymers, in: Proceedings of the Polymer Processing Society 30th Annual Meeting, 2014: p. 5.

[3] D. Tasch, A. Mad, R. Stadlbauer, M. Schagerl, Thickness dependency of mechanical properties of laser-sintered polyamide lightweight structures, Additive Manufacturing. 23 (2018) 25–33. https://doi.org/10.1016/j.addma.2018.06.018.

[4] I.V. Shishkovsky, Thermoviscoplasticity of powder composition under selective laser sintering, in: V.Y. Panchenko, V.S. Golubev (Eds.), Vladimir, Suzdal, Russia, 2002: p. 446. https://doi.org/10.1117/12.464180.

[5] A. Wegner, Theorie über die Fortführung von Aufschmelzvorgängen als Grundvoraussetzung für eine robuste Prozessführung beim Laser-Sintern von Thermoplasten, Universitätsbibliothek Duisburg-Essen, 2015.

[6] D. Drummer, M. Drexler, K. Wudy, Derivation of heating rate dependent exposure strategies for the selective laser melting of thermoplastic polymers, in: Cleveland, Ohio, USA, 2015: p. 160006. https://doi.org/10.1063/1.4918513.
[7] M. Launhardt, Zur Entstehung von Dimensionen und Maßabweichungen beim Laserstrahlschmelzen von Kunststoffen, FAU University Press, Erlangen, 2021.
[8] S.-L. Sindinger, C. Kralovec, D. Tasch, M. Schagerl, Thickness dependent anisotropy of mechanical properties and inhomogeneous porosity characteristics in laser-sintered polyamide 12 specimens, Additive Manufacturing. 33 (2020) 101141. https://doi.org/10.1016/j.addma.2020.101141.
[9] M. Launhardt, D. Drummer, Determination of the fundamental dimension development in building direction for laser-sintered parts, Journal of Polymer Engineering. 39 (2019) 197–206. https://doi.org/10.1515/polyeng-2018-0204.
[10] S. Greiner, A. Jaksch, S. Cholewa, D. Drummer, Development of material-adapted processing strategies for laser sintering of polyamide 12, Advanced Industrial and Engineering Polymer Research. (2021) S2542504821000294. https://doi.org/10.1016/j.aiepr.2021.05.002.
[11] A. Wörz, D. Drummer, Understanding hatch-dependent part properties in SLS, in: Proceedings of the 29th Annual International Solid Freeform Fabrication Symposium 2018, Austin, Texas, US, 2018: pp. 1360–1369.
[12] A. Wörz, Zu schichtabhängigen Struktur-Eigenschaftsbeziehungen von LS-Bauteilen, doctoralthesis, Friedrich-Alexander-Universität Erlangen-Nürnberg (FAU), 2021.
[13] W. S. Slaughter, The linearized theory of elasticity. Springer Science & Business Media, 2012.
[14] M. Bischoff, K. U. Bletzinger, W. A. Wall, E. Ramm, Models and finite elements for thin-walled structures. Encyclopedia of computational mechanics, 2004.
[15] M. Masmali, P. Mathew, An analytical approach for machining thin-walled workpieces. Procedia Cirp, 2017: pp. 187-192.
[16] H. Brezis, Convolution and regularization. In: Functional Analysis, Sobolev Spaces and Partial Differential Equations. Springer, New York, NY, 2011: pp. 104-111.
[17] DIN EN ISO 527-1: 2019-12 Kunststoffe – Bestimmung der Zugeigenschaften – Teil 1: Allgemeine Grundsätze (ISO 527-1:2019); Deutsche Fassung EN ISO 527-1:2019 (Plastics – Determination of tensile properties – Part 1: General principles (ISO 527-1:2019); German version EN ISO 527-1:2019), Berlin: Beuth Verlag.
[18] DIN EN ISO 527-2: 2012-06 Kunststoffe – Bestimmung der Zugeigenschaften – Teil 2: Prüfbedingungen für Form- und Extrusionsmassen (ISO 527-2:2012); Deutsche Fassung EN ISO 527-2:2012 (Plastics – Determination of tensile properties – Part 2: Test conditions for moulding and extrusion plastics (ISO 527-2:2012); German version EN ISO 527-2:2012), Berlin: Beuth Verlag.
[19] S. Greiner, K. Wudy, A. Wörz, D. Drummer, Thermographic investigation of laser-induced temperature fields in selective laser beam melting of polymers, Optics & Laser Technology. 109 (2019) 569–576. https://doi.org/10.1016/j.optlastec.2018.08.010.
[20] E. M. Stein, G. Weiss, Introduction to Fourier Analysis on Euclidean Spaces (PMS-32), Volume 32. In: Introduction to Fourier Analysis on Euclidean Spaces. Princeton University Press, 1971.
[21] G. Leoni. A first course in Sobolev spaces. American Mathematical Soc., 2009.
[22] J. Rust, Using randomization to break the curse of dimensionality. Econometrica: Journal of the Econometric Society, 1997: pp. 487-516.
[23] W. Rudin, Principles of mathematical analysis. McGraw-Hill, New York, 1976.
[24] H. J. Weber; G. B. Arfken, Vector Analysis in Curved Coordinates and Tensors. In: Essentials of math methods for physicists. Academic Press, 2013: pp. 103-141.
[25] R. Burden, J. Faires, Numerical analysis. Brooks/Cole Cengage Learning, Boston, 2011.
[26] D. G. Luenberger, Least-Squares Estimation. In Optimization by Vector Space Methods. John Wiley & Sons, New York, 1969: pp. 78–102.
[27] E. DiBenedetto, Real Analysis. Birkhäuser, Boston, 2002.